# Shock Propagation in Deuterium–Tritium–Saturated Foam

## Introduction

Over the past few years there has been considerable interest regarding the use of foam shells in inertial confinement fusion (ICF)[1] targets. The original proposed use of plastic foam shells was as a matrix for liquid deuterium–tritium (DT) fuel.[2] More recently, in the designs of Colombant *et al.*,[3] foam has been proposed for use as an ablator material, in conjunction with an outer layer of a high-atomic-number material such as Pd. In these designs, the foam is preheated by radiation from the outer layer and has substantially higher ablation velocities, resulting in a more-stable outer surface. In other high-gain "wetted-foam" designs,[4] the foam is used primarily because it has a higher atomic number than DT. This results in greater absorption and increased laser-energy coupling, which in turn allows more fuel to be used without reduction in stability, resulting in higher gain. Sophisticated target designs for inertial fusion energy (IFE) that build on these techniques and use wetted-foam layers have been designed and tested computationally (see, for instance, Ref. 5 and references therein). Foam has also been suggested to reduce laser imprint in direct-drive ICF.[6]

Direct-drive ICF target designs use a pulse that drives at least two main shocks into the target. Target performance depends in part on the timing of these shocks. The first shock propagating through a foam layer encounters an inhomogeneous medium. It is important to know whether this will have any effect on the shock speed and resulting shock timing. In addition, inhomogeneities in the foam can feed through to the shell's inner surface,[7] and again to the outer surface, where they may potentially contribute to seeds of hydrodynamic instability during the deceleration and acceleration phases of the implosion (respectively).

The length scale of the foam inhomogeneities is a fraction of a micron; for one of the foams discussed here, the foam is fibrous, with a fiber radius of about 1/20 $\mu$m. A National Ignition Facility[8] direct-drive target radius is much larger, at least 1.5 mm, with a shell thickness of hundreds of microns. This large range of length scales makes it prohibitive to model foam inhomogeneities in a simulation of a target implosion. As a result, simulations of foam-target implosions must model the wetted foam as a homogeneous mixture.

To investigate the effects of foam microstructure, we have performed two-dimensional (2-D) hydrodynamic simulations of a shock propagating through a plastic foam saturated with DT ice. In these simulations, the microstructure of the foam filaments is resolved, allowing determination of its effects on shock behavior. ICF-relevant wetted-foam simulations modeling the foam microstructure have been performed previously by Phillips,[9] Hazak *et al.*,[10] Kotelnikov and Montgomery,[11] and Philippe *et al.*[12] Phillips considered an ICF-relevant case of a shock propagating through a random arrangement of plastic (CH) fibers filled with DT. He found that the shock-front perturbations were comparable in size to the fiber radius, and that the kinetic energy in the mixing region—the post-shock region in which the foam and DT are mixed and potentially homogenized—accounts for of the order of a few percent of the mean kinetic energy. Hazak *et al.* performed 2-D simulations of a shock propagating through a regular array of CH fibers, filled with liquid deuterium ($D_2$). They focused on the mix region behind the shock, deriving generalized jump conditions including fluctuations. Among other results, they found that the fluctuations result in an under-compression behind the shock, and that the jump to the under-compressed state cannot be modeled by a simple change in the ratio $\gamma$ of specific heats. Kotelnikov and Montgomery also simulated a regular array of fibers, saturated with cryogenic DT. In their simulations they made use of a kinetic-theory–based computational model. Like Hazak *et al.*, they found that the inhomogeneities result in a post-shock mixing region in which energy is temporarily stored in turbulent motion. Finally, Philippe *et al.* performed simulations of DT-saturated foams using an adaptive-mesh-refinement code and allowing random fiber placement. They focused on the effects of inhomogeneities on the shock speed for a low- and high-density foam. They found that for the high-density foam, the deviation in shock speed from the homogeneous value was about 1% and less than 0.3% for the low-density foam.

This problem has also been addressed in astrophysical contexts, where the ratio of the material densities is much larger. The role of clumps in augmentation of the Rayleigh–Taylor instability in supernova remnants was studied using hydrodynamic simulations by Jun.[13] More recently, Poludnenko *et al.*[14] have simulated the interaction of a shock with a layer of circular obstructions, or clumps, determining the critical inter-clump distance required for the transition to a non-interacting regime in which the clouds are destroyed by the shock independently of one another. They also discussed mass loading as well as the effects of finite layer thicknesses for the collection of circular obstructions.

In our simulations the shock passage through a random array of CH fibers separated by DT is simulated, and the time-averaged level of fluctuations is determined as a function of distance behind the shock front for quantities of interest. We define the decay length for a quantity as the inverse of the logarithmic derivative of the quantity's perturbations [see Eq. (1)]. We will show that the decay lengths are comparable to a micron for a wide range of foam densities. For shock propagation distances characteristic of ICF targets, the average post-mixing region conditions approach those given by the Rankine–Hugoniot jump conditions. We also address questions of feedthrough and feedout, showing that the stability of the shock front once it leaves the wetted-foam layer minimizes the effect of feedthrough.

In the following sections (1) the hydrodynamic code used and the simulations that were performed are described; (2) the interaction of a shock with a single circular obstruction is discussed; (3) the results of multifiber simulations and their implications are presented; (4) the role of the pusher (i.e., the inflow boundary conditions) is discussed; and (5) our conclusions are presented.

## Numerical Simulations

The code used for these simulations, *AstroBEAR*,[15] is based on the adaptive-mesh-refinement (AMR) code *AMRCLAW*.[16] In the AMR approach, subregions of the computational domain are provided with higher resolution according to a refinement criterion such as the magnitude of the truncation error or the local gradients of the hydrodynamic variables. Because the entire simulation region is not simulated at the highest resolution, the AMR scheme typically provides much-reduced execution times. In this implementation of AMR, the code attempts to optimally gather the refined cells into rectangular subgrids in order to minimize the overhead associated with refinement, and subsequently the hydrodynamic equations are advanced in each grid and on every refinement level. The refinement criterion used in *AstroBEAR* is Richardson extrapolation, in which cells are flagged for refinement based on a local estimation of the integration error. *AstroBEAR* employs a fully nonlinear Riemann solver with the second-order-accurate Wave-Propagation Algorithm integration scheme of LeVeque.[17] A polytropic equation of state is used with a ratio of specific heats $\gamma = 5/3$ gas. Thermal and radiative energy transport are not modeled in these simulations. We expect that in a real target implosion these mechanisms will dissipate fluctuations in the post-shock mix region. The results of our simulations will thus overestimate the size of the post-shock mix region and underestimate the fluctuation decay rate behind the shock. The effects of radiation could in principle be imitated by elevating the initial fiber pressure to model the absorption by the fibers of radiation emitted from the corona.

*AstroBEAR* tracks multiple materials by solving separate continuity equations for each of the materials—the fiber material and the DT—which provides a measure of the level of mixing after the shock (this is referred to as volume-fraction contouring).[18] There is no interface construction at the boundary between the two materials. Instead, the mass of each material is maintained for a given cell. For instance, consider two adjacent cells, the left containing the first material at a higher pressure and the right the second material at a lower pressure. After one time step, the boundary between the two materials will have moved into the right cell, and at the end of that time step the right cell will be considered to contain a uniform mixture of both materials, with the appropriate fractions. Material interfaces experience some degree of smearing as a result. Shock-tube tests indicate that on the time scale of these simulations, the material interface is spread out over a distance approximately equal to the initial fiber radius. This method of material tracking is passive and in no way affects the hydrodynamics behind the shock, or the decay of perturbations in the mix region.

*AstroBEAR* solves the Euler equations, making no provision for turbulent motion. The Reynolds number is $\mathrm{Re} = UL/\nu$, where $U$ is a characteristic flow speed, $L$ is a characteristic length scale, and $\nu$ is the viscosity coefficient. For a shock in wetted foam, we may take for the length scale $L$ the fiber radius $a$ (~1/20 $\mu$m for the foam density of interest), and for the characteristic flow speed $U$ the post-shock flow speed $u$ (~30 km/s is a characteristic post-shock speed). Following Robey,[19] we may estimate the kinetic viscosity using the model of Clerouin *et al.*[20] The initial shock strength and electron and ion conditions for the high-gain, direct-drive, NIF wetted-foam design described in Ref. 4, determined by 1-D simulations using *LILAC*,[21] give a Reynolds number of ~2800. This is below the value of 7700 typically taken as the critical value for the onset of turbulence. In our simulations no artificial viscosity is used, although a similar effect is obtained by splitting the contact discontinuity according to the scheme of Robinet *et al.*[22] This is done to prevent the growth of unphysical features (often referred to as "carbuncles"). Care has been taken to ensure that physical features are not damped.

As mentioned above, wetted-foam target designs, such as the one described in Ref. 4, take advantage of the higher laser absorption of plastic fiber than pure DT. In these designs a low-density plastic foam, which has a dry-foam density of ~140 mg/cc, is saturated with DT ice, e.g., $CH(DT)_4$, raising its density to 360 mg/cc. A typical direct-drive, NIF-scale target design consists of a shell of DT ice surrounded by a thin layer of plastic. In a wetted-foam design, an outer portion of the DT shell is replaced by wetted foam. The thickness of this layer is chosen so that the foam is entirely ablated by the laser pulse. In choosing the density of the foam, a balance must be struck between the increased absorption, which is greater for larger densities, and minimizing the radiative preheat of the inner-fuel layer of the DT ice, which is also greater for larger foam densities. As in many direct-drive target designs, the pulse consists of an initial intense picket, followed by a foot pulse, and then a drive pulse. The picket/foot combination launches the first shock into the shell, creating a greater adiabat in the ablator than in the inner-fuel layer. The second shock, launched by the more-intense drive pulse, is timed to meet the first shock inside the gas within the shell. The first shock is most relevant here since it is the only shock to encounter unshocked and unmixed wetted foam.

We have performed a number of simulations to investigate the effects of microstructure on shock propagation. The baseline simulation consists of an 8-$\mu$m × 0.8-$\mu$m simulation region filled with a mixture of DT (with a density of 0.253 g/cc) and randomly placed polystyrene (CH) fibers (with a density of 1.044 g/cc). The foam being simulated, resorcinol formaldehyde (RF), is a fibrous foam with fiber spacing of ~0.1 to 0.2 $\mu$m. For RF, denser foams generally have the same average center-to-center fiber separation, but with thicker fibers. We simulate a foam that has a random array of fibers with the same average density as a rectangular array of fibers with a unit cell size of $R = 0.2$ $\mu$m. This corresponds to an average nearest-neighbor distance of $d \sim 0.13$ $\mu$m (so the simulation size is ~60 $d$ × 6 $d$). The combination of fiber density and average density, for a given fiber spacing, determines the fiber radius: for $CH(DT)_4$ the fiber radius is $a \sim 0.0428$ $\mu$m. The dry-foam density $\rho_{\text{dry}}$ and wetted-foam density $\rho_{\text{ave}}$ are related by $\rho_{\text{ave}} = \rho_{\text{dry}} + \rho_{\text{DT}} - \rho_{\text{dry}}\rho_{\text{DT}}/\rho_{\text{CH}}$. The dry-foam density is given by $\rho_{\text{dry}} = \rho_{\text{ch}}\pi(a/R)^2$. In these simulations generally two levels of refinement, both ×4 (so that a cell being refined is replaced by 16 cells in a 4 × 4 grid), were used in addition to the base level. The cells have an aspect ratio of unity, with a resolution at the highest level of 800 cells/$\mu$m, and an equivalent simulation size at the highest resolution of 6400 × 640. This corresponds to about 68 cells across a fiber. We find negligible differences between 34 and 136 cells per fiber radius. This convergence is supported by a resolution scan performed using *AstroBEAR* by Poludnenko *et al.* [Ref. 23; see their Fig. 3(a)], who also found only small differences between 32 and 64 cells per fiber radius.

In addition to this simulation size, we have also performed simulations with a size of 0.2-$\mu$m transverse to the shock propagation direction, but with a 16-$\mu$m-simulation region length in the direction of shock propagation, in order to extend the size of the mixed region. The upper and lower boundary conditions in these simulations are periodic, so the central difference between these simulations is that in the thinner one the lateral distance between the fibers is always 0.2 $\mu$m.

If we take the ablation-driven shock to travel to the right, then the right simulation boundary condition is outflow, or zero-order extrapolation, and the left is inflow. The inflow conditions are given by the Rankine–Hugoniot conditions for the average pre-shock density and pressure and for a post-shock pressure of 8 Mbar. We refer to this as an "impedance-matched" boundary condition [other inflow boundary conditions are discussed in the **Results for Different Pushers** section (p. 237)]. The CH and DT are initially in pressure equilibrium with a pressure of 0.01 Mbar. The flow, being governed by the Euler equations, is independent of Mach number when in the strong-shock limit,[24] so that the results are not sensitive to the initial pressure.

## The Interaction of a Shock with a Single Fiber

The interaction of a shock with a single fiber (or circular obstruction) has been studied extensively as a hydrodynamic problem.[25,26] Additional physical elaborations have also been modeled, such as partial ionization[27] and magnetized obstructions (see, e.g., Ref. 28). Following Klein *et al.*,[24] the interaction of a shock with a fiber may be broken down into several distinct phases. If the flow were one-dimensional, a "forward" shock would propagate through the fiber, compressing and impulsively accelerating it, while a "reverse" bow shock would be reflected back into the DT. Once the forward shock had crossed the fiber, a rarefaction wave would be sent back across the fiber, followed by a continuous period of acceleration that would continue until the fiber speed equaled that of the surrounding shocked DT.

Because the flow is two-dimensional, the fiber experiences several shocks: In addition to the main forward shock, other shocks are driven into the fiber from the sides as the shock in the DT moves around and past the fiber. Similarly, many rarefaction waves (RW's) are launched as each of these shocks breaks out of the fiber. These additional rarefaction waves result in expansion during this phase, both in the direction of and perpendicular to the direction of shock propagation. Finally, following the passage of these RW's, the fiber begins to accelerate. During this phase, the fiber is accelerated to the speed of the ambient (DT) fluid flow.

As described in Ref. 25, the passage of the shock generates, for a cylindrical fiber, two vortex lines behind the obstruction, and for a spherical obstruction a vortex ring is generated. These vortices and the vorticity generated by the shear flow as the fiber is accelerated mix the fiber and interfiber material. For a cylindrical obstruction and a normal shock (whose velocity vector is normal to its surface), the vortex lines are of equal magnitude and oppositely directed, so the total vorticity remains zero. If the shock is oblique, the symmetry is broken and net vorticity may be generated.

The fiber is subject to the Richtmyer–Meshkov instability as the shock first passes. As the fiber is accelerated to the speed of the post-shock DT, it is also subject to the Rayleigh–Taylor (RT) instability and, due to the shear at the fiber boundaries, the Kelvin–Helmholtz (KH) instability. In the case of a CH fiber and DT ambient fluid, the density ratio is $1.044\ \mathrm{g\,cc^{-1}}/0.253\ \mathrm{g\,cc^{-1}} \sim 4$. Both the RT and KH instabilities are more effective at mixing the fiber and ambient material when the ratio of fiber to ambient density is greater. Figure 100.1 shows the density at three times for a fiber of radius 0.0428 $\mu$m struck by a 3-Mbar shock, for a fiber-to-interfiber mass density ratio of 4:1. A measure of the fiber's mixing or destruction time may be made by determining the fraction of fiber material that lies outside the initial radius of the fiber from its center of mass (this is shown in Fig. 100.2). If we take the fiber destruction time as the time it takes for the flow to expel 75% of the fiber material from this region, we see that the fiber is destroyed in ~13 ps.

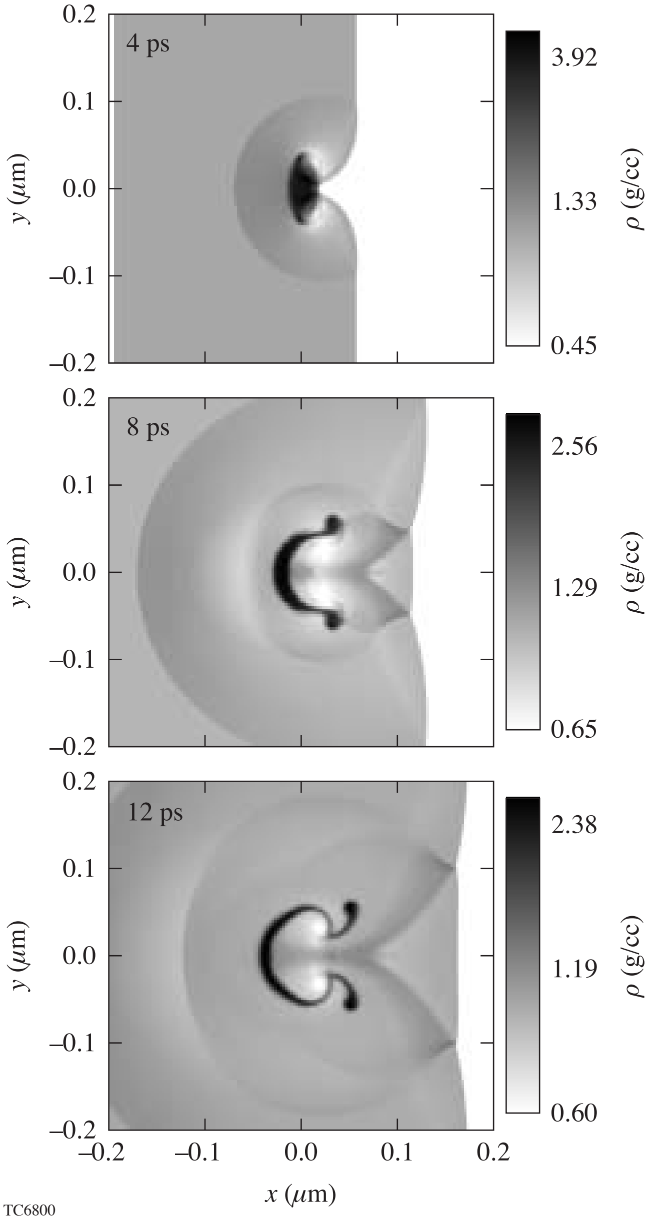

Figure 100.1
Density profiles at 4, 8, and 12 ps for a Mach-24 shock interacting with a CH fiber. The density ratio is 4:1.

## The Interaction of a Shock with Many Fibers

Consider now the case of a shock driven into a field of randomly placed fibers. Here the shocked fibers interact with one another, creating a "mix" region in which the post-shock vorticity mixes the CH and DT. The density $\rho(x, y)$ at 96 ps is shown in Fig. 100.3(a) for a $\mathrm{CH(DT)_4}$ wetted foam struck by an 8-Mbar shock with impedance-matched inflow boundary

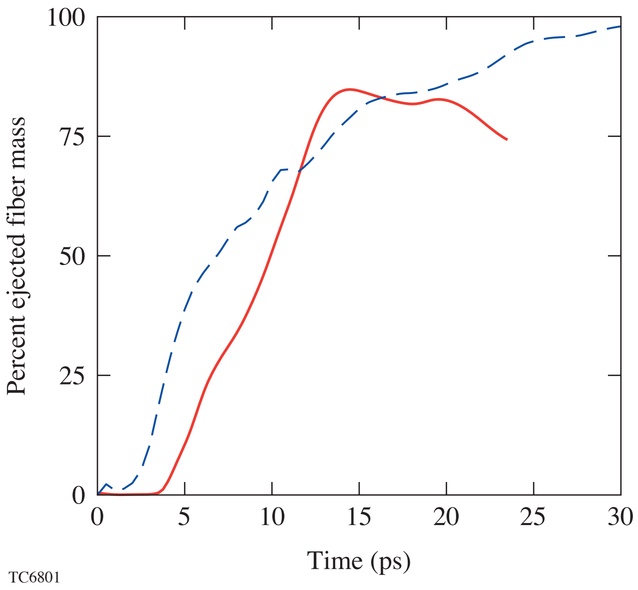

Figure 100.2
The fraction of fiber mass that lies outside the original fiber radius of the fiber's center of mass as a function of time. As the fiber material is mixed with the ambient material, it is flung outside of its original boundaries. The solid line is a single fiber with a 4:1 density ratio with the interfiber material (see Fig. 100.1). The dashed line is from a simulation of fiber destruction in the presence of other fibers. Taking the 75% mark as an arbitrary measure of fiber destruction, the fiber is destroyed after ~12.3 ps for a single fiber and ~13.5 ps in the presence of other fibers, although in this case the fiber destruction is much more thorough.

conditions. As was shown in Ref. 14, if the interfiber distance is sufficiently large, the fibers enter a noninteracting regime where the fibers are destroyed before they expand far enough to interact with one another. The parameters of interest here are in the interacting regime. The CH fiber density $\rho_{CH}$ alone is shown in Fig. 100.3(b). The dual-vortex motion and the resulting mushroom-shaped features due to shock passage can be seen in Fig. 100.3(b). From this figure we see that CH and DT, which are clearly distinct at the shock front (the dotted line at ~5.4 $\mu$m), are well mixed by the end of the mix region (at ~4 $\mu$m). We also note from this figure that there is a thin region between the shock front at ~5.4 $\mu$m and the shocked fibers (~5.3 $\mu$m at $y = 0.2$ $\mu$m). This gap between the shock and the entrained shocked CH is due to the finite time the post-shock flow takes to accelerate the fibers to the post-shock speed. In this region the average density, being primarily that of the shocked DT, is lower than in the rest of the mix region, contributing to an initial under-compression behind the shock.

Figure 100.2 shows that when a fiber is mixed in the presence of other fibers, the mixing proceeds more quickly initially and is more thorough (see also Ref. 14). For the simulation used here, the ejected fiber mass asymptotes near 100%. The degree of mixing may be demonstrated by designating one of the fibers as a third species identical physically to CH but maintained as a separate material numerically. Figure 100.4 shows contours of density for a particular fiber (solid lines), as well as the total density (grayscale). By 120 ps, the outermost contour, which represents 10% of the peak density, contains a volume of 0.063 $\mu$m$^2$. This is comparable to the specific volume 0.04 $\mu$m$^2$ of the fibers for this initial spacing.

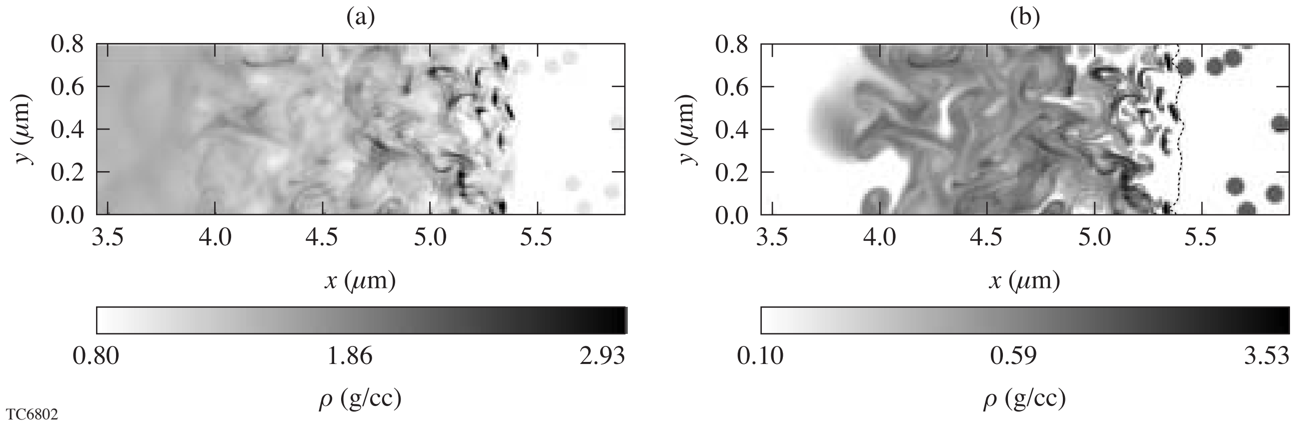

Figure 100.3
The total density (a) and CH density (b) at 96 ps for an 8-Mbar shock driven into wetted foam. The dotted line in (b) shows the location of the shock front.

The mix region is also the source of the bow shocks reflected when the main shock encounters the fibers. These shocks eventually propagate away from the main shock and out of the mix region. The fluctuations in density, pressure, and transverse velocity can be seen in their $y$ averages—$\overline{\rho}$, $\overline{p}$, and $\overline{u}_y$—shown in Fig. 100.5 for the simulation of size 16 $\mu$m × 0.2 $\mu$m. (A horizontal bar is used to indicate an average over the $y$ coordinate.) The mixing flow, due to the reflected shocks and the post-shock vorticity, is generally both horizontal—parallel to the shock motion—and vertical. The vertically moving shocks are unsupported since the flow supporting the shock is entirely horizontal. The vertical shocks, then, decay as the shocked fibers sink into the mix region. In addition, since on average the upward-moving shocks will have the same strength as the downward-moving shocks, one might expect the net vertical speed once these have passed to be approximately zero. Because of the random fiber placement, though, some vertical motion remains behind the shock [Fig. 100.5(c)]. In the 0.2-$\mu$m-wide simulation, the periodic upper- and lower-boundary conditions, combined with the small vertical simulation size, mean that vertical motion as large as 10 $\mu$m/ns remains, even several microns behind the shock. In the 8-$\mu$m × 0.8-$\mu$m simulation, $\overline{u}_y$ in the mix region is smaller. This is because in the wider simulation there are fibers for a transverse shock to encounter other than the fiber that created it.

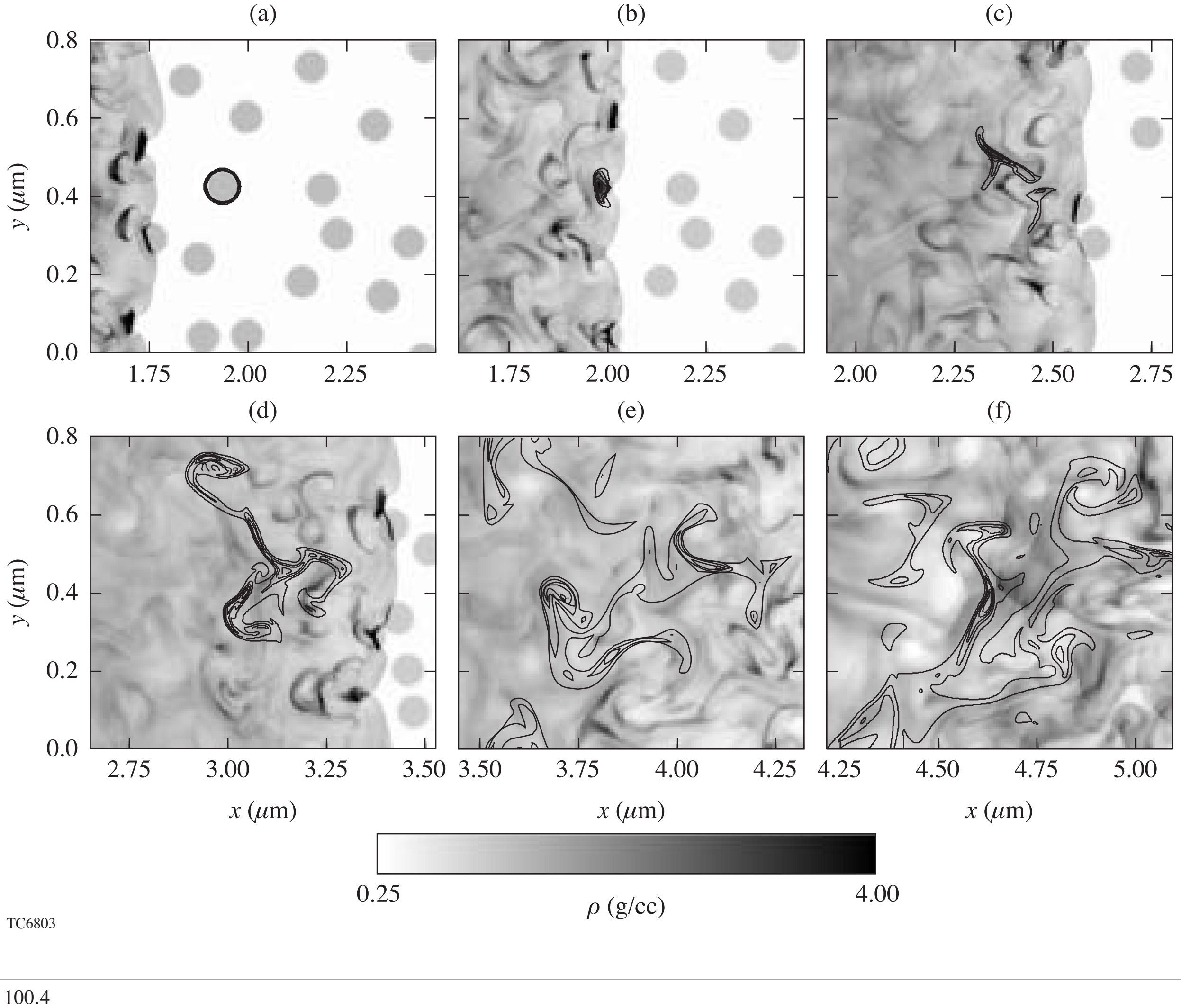

Figure 100.4
The total mass density (grayscale) and the mass density (lines) of material from a "tagged" fiber initially at $x = 1.93$ $\mu$m and $y = 0.42$ $\mu$m. The contour levels for the tagged fiber correspond to 10%, 32.5%, 55%, and 77.5% of the peak tagged-fiber density. The frames are from (a) 30 ps, (b) 35 ps, (c) 45 ps, (d) 60 ps, (e) 80 ps, and (f) 100 ps.

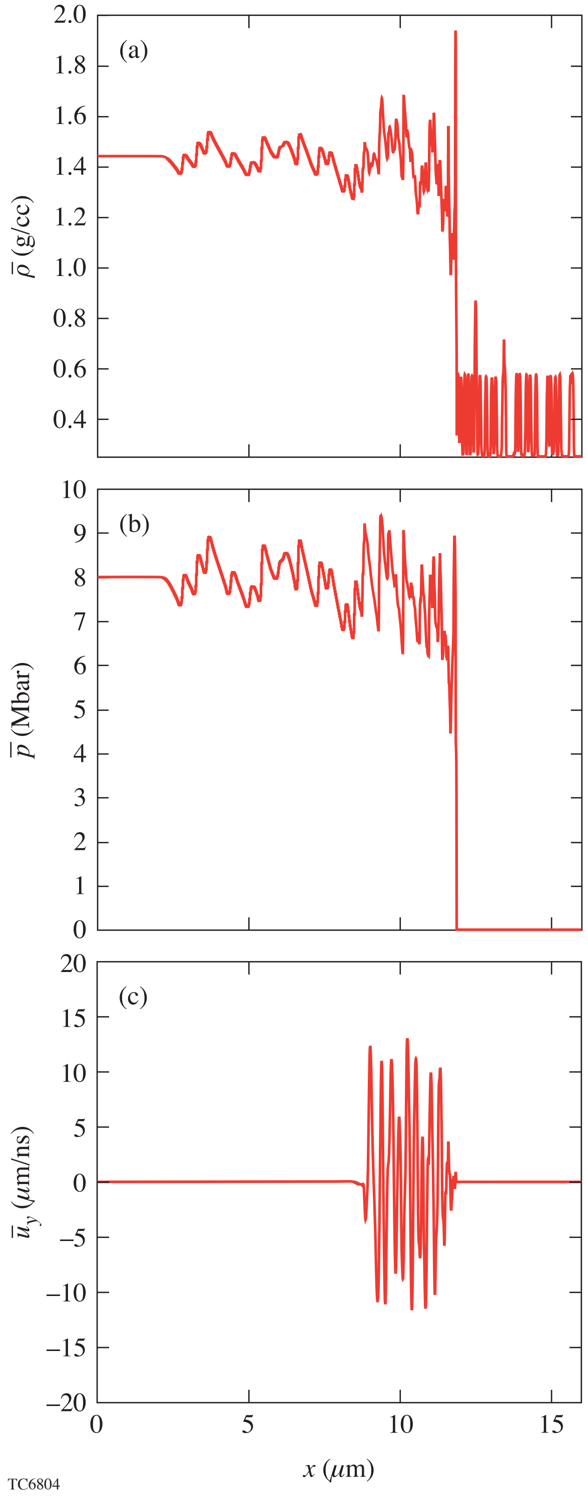

Figure 100.5
The $y$-averaged density (a), pressure (b), and $y$ velocity (c) at 300 ps for a 16-$\mu$m × 0.2-$\mu$m simulation.

To quantify this we have calculated average quantities related to the flow behind the shock. The mix region is given approximately by the region bounded on the right by the shock $x_s(y;t)$ (assuming the shock is a single-valued function of $y$) and on the left by the interface between the pusher (or inflowing material) and the shocked wetted foam, $x_i(y;t)$, as is shown in Fig. 100.6. If the wetted-foam layer is preceded by a CH layer, for instance, then there will be a contact discontinuity at the pusher/foam interface, where the density jumps but the pressure is constant. The location of the fiber material in the mix region is shown in Fig. 100.3(b), demonstrating that the vorticity quickly mixes the CH and the DT behind the shock front. For small fiber-to-DT density ratios the fluctuations in the shock-front position as a function of $y$ are small enough to allow us to define an average shock position $\bar{x}_s(t)$. The average pusher location $\bar{x}_s(t)$ is given, for a strong shock with $\gamma$ = 5/3, approximately by $\bar{x}_i \approx \bar{x}_s(t=0)+3\bar{D}t/4$, where $\bar{D}$ is the average shock speed. The interface position may be inverted to give the time $\bar{t}_i(x)$ when the interface is a distance $x$ behind the shock. The time average of a flow variable $q$, from when it is

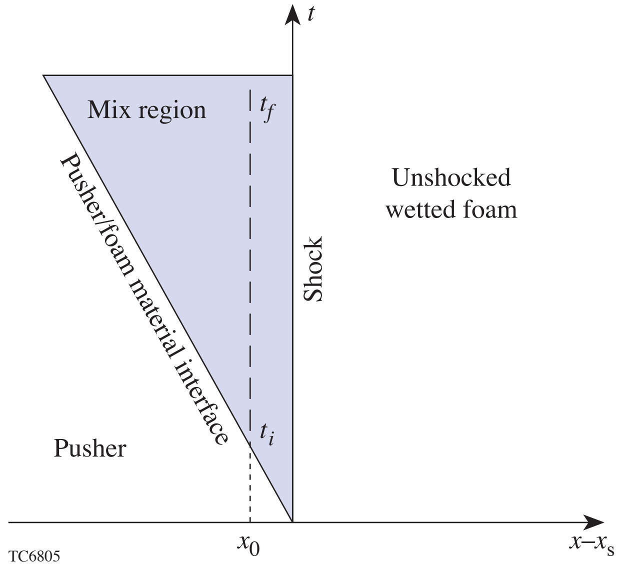

Figure 100.6
The mix region (shaded), pusher, and unshocked material are shown as a function of time, in the frame of the main shock. The time averages are computed of the flow variables in the mix region between the shock and the pusher as functions of the distance behind the shock. For instance, the time average at a distance $x_0$ behind the shock is found by averaging from time $t_i$ to time $t_f$.

first shocked to some final time $t_f$, as a function of the distance $x$ behind the shock, is then

$$\langle\bar{q}\rangle(x)=\left[t_f-t_i(x)\right]^{-1}\int_{t_i(x)}^{t_f}\bar{q}(x,t)\,dt,$$

where $\bar{q}$ is the average of $q(x,y)$ over $y$ and brackets are used to indicate this *mixing-depth average*. The distance $x$ behind the main shock front may be thought of as a depth within the mix region. The mixing-depth average can also be taken of any quantity independent of $y$, such as $q_n$, the $n$th Fourier-mode amplitude of some variable $q$, in the $y$ direction, or $q_{\text{rms}}$, the root-mean-square (rms) deviation of $q$ as a function of $y$. This double average $\langle\bar{q}\rangle$ is meaningful when the flow reaches a steady state in which the average behavior of the fluctuations as a function of distance behind the shock is roughly constant in time. We have found this to be the case after the initial stages of our simulations. Note that the averaging time is inversely proportional to the distance from the shock front, so the statistical fluctuations tend to be larger for greater distances from the main shock front. The mix-depth averages of the root-mean-square variations in the $y$ direction are shown for the pressure, the density, and the ratio of kinetic energy (in the pre-shock frame) to total energy $E_{\text{kinetic}}/E_{\text{total}}$, and $u_y$ in Fig. 100.7, for the 8-$\mu$m × 0.8-$\mu$m and 16-$\mu$m × 0.2-$\mu$m simulations discussed above. The decay scale length

$$L_q = dx/d\,\ln\langle q_{\text{rms}}\rangle \tag{1}$$

just behind the shock in the mixing region for these variables is comparable to 1 $\mu$m for this foam density. The relative Fourier-mode amplitudes of modes 1 to 6 of the pressure (not shown) remain roughly constant with mix-region depth, suggesting that the power is not moving to shorter or longer wavelengths, but decaying uniformly at a rate independent of mode number.

The rms amplitudes for a simulation of the same size but 50%-higher resolution are approximately equal to those in Fig. 100.7, indicating resolution convergence. Since the rate of decay of fluctuations is independent of resolution, the decay is not due to numerical losses, but to the mechanisms described above. When viscosity is negligible, the circulation in a given region is conserved according to Kelvin's circulation theorem (see, for instance, Ref. 29); in effect, vortices are "frozen" into the fluid and are advected with the flow. For the case of cylindrical fibers, as mentioned above, the vortices are created in opposing pairs with no net average vorticity generation. As

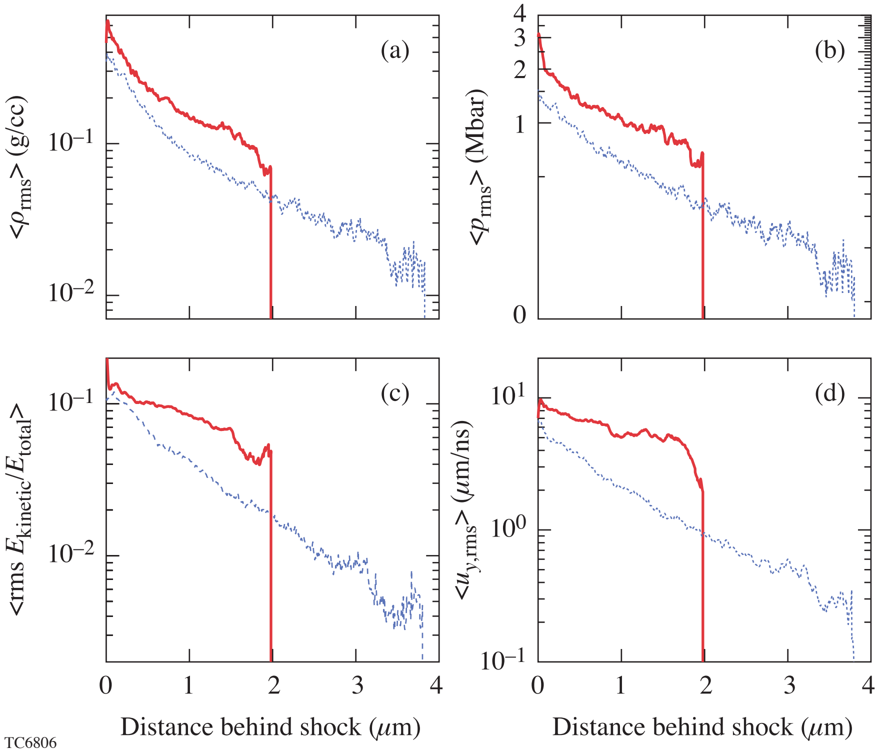

Figure 100.7
The rms variations of the time-averaged density (a), pressure (b), fraction of kinetic energy (in the pre-shock frame) (c), and vertical velocity (d) as functions of the distance behind the shock. These show a decay length comparable to 1 $\mu$m for this foam density.

the vortices interact behind the shock, they are free in time to mix, but not decay, because of the absence of physical viscosity and the small size of the numerical viscosity. The level of mixing can again be gauged qualitatively by Fig. 100.4. In the 16-$\mu$m simulation the mixing is sufficient to reduce the time average of the rms variations to 1.2% for $\rho$, 1.8% for $p$, and 0.9% for $E_{\text{kinetic}}/E_{\text{total}}$, of the average values.

The pressure decay length [Eq. (1)] behind the shock as a function of foam density is shown in Fig. 100.8. These values are taken from simulations that have a simulation region of $8 \times 0.2$ $\mu$m and an equivalent grid size of $6400 \times 160$. The error bars in this plot are given by the linear regression used to calculate the mixing length. Poludnenko *et al.* found,[14] for simulations with a larger ratio of fiber to interfiber density, that the mixing was more efficient when the average minimum interfiber distance was less than a critical distance. We find the same result: for dry-foam densities less than ~75 mg/cc, for which the interfiber distance is ~6.6 times the fiber radius, the mixing length is about 1.2 $\mu$m, as opposed to about 0.8 $\mu$m for higher densities. The difference between the interacting and noninteracting regimes is illustrated by considering the vorticity generated by the shock. This is shown in Fig. 100.9 for three foam densities—25, 75, and 150 mg/cc—for about the same shock position. For these three densities, as mentioned above, the average distance from fiber center to fiber center is the same, but the fibers are of different sizes. The fiber radius is given by $a = R\left[\rho_{\text{dry}}/\left(\pi\rho_{\text{CH}}\right)\right]^{1/2}$, so these densities correspond to fiber radii of 0.0175 $\mu$m, 0.0302 $\mu$m, and 0.0428 $\mu$m. For 25-mg/cc density, the vortex dipoles associated with each fiber remain paired and intact for much longer before interacting with other neighboring vortex dipoles. In contrast, for 150 mg/cc, the dipole length increases much more quickly, resulting in greater mixing.

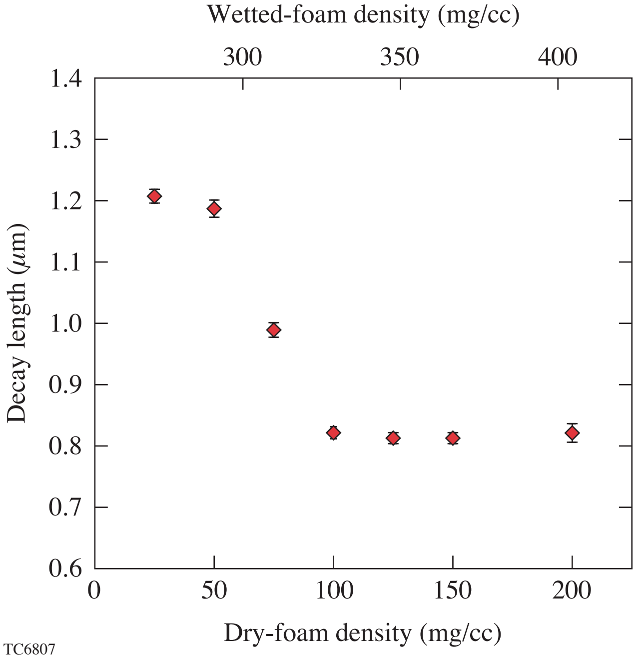

Figure 100.8
The decay length behind the shock as a function of foam density. The decay length is approximated by the scale length of the time-averaged decay of pressure variations just behind the shock. The error bars are given by the uncertainty in the exponential fit.

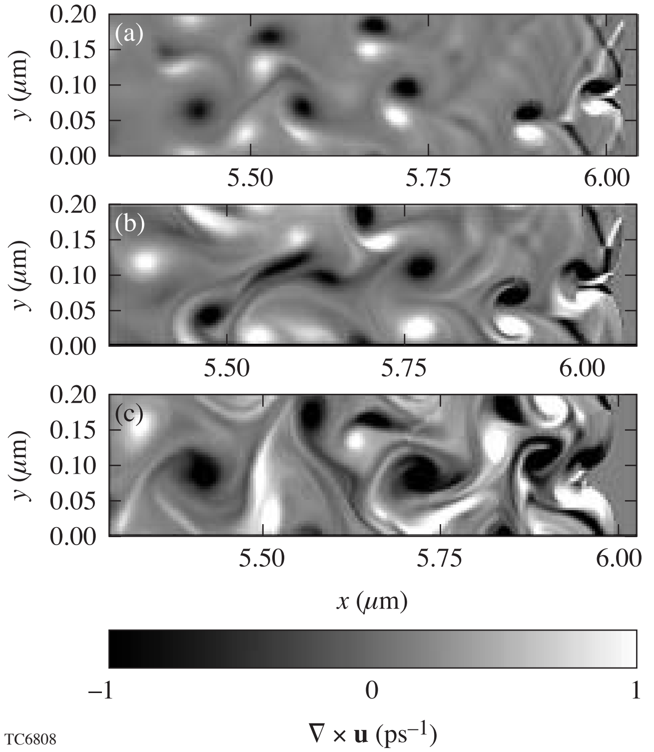

Figure 100.9
The vorticity is shown as the shock reaches ~6 $\mu$m for three dry-foam densities: (a) 25, (b) 75, and (c) 125 mg/cc. The average interfiber distance is the same in all three cases, while the fiber radius is larger for higher foam densities.

The Rankine–Hugoniot conditions represent conservation of energy, momentum, and mass for a steady flow of polytropic gas in the absence of transverse motion. The RH jump conditions will be met over a region only to the degree that (1) the shock is steady; (2) the flow in and out of the region is steady; (3) the fluctuations at the left and right boundaries are uncorrelated (e.g., $\left\langle \overline{\rho u_x} \right\rangle = \left\langle \overline{\rho} \right\rangle \left\langle \overline{u}_x \right\rangle$; see Ref. 10); and (4) the turbulence and transverse motion have decayed at the downstream boundary. The shock steadiness is given by the error of the linear regression used to determine the shock speed; for the 16-$\mu$m simulation, the speed is 54.32 $\mu$m/ns±0.033 $\mu$m/ns—an uncertainty of 0.12%. As mentioned above, the post-shock flow is approximately steady. The pre-shock flow is approximately steady when averaged over time scales much longer than the characteristic time scale for the inflowing density fluctuations, which is given by the time it takes the shock to move from one fiber to the next, ~$d/D$. For an 8-Mbar shock and a dry-foam density of 150 mg/cc, the shock speed is ~50 $\mu$m/ns, and the averaging time must be longer than ~4 ps. The duration of the 16-$\mu$m simulation is, for instance, ~300 ps. The fluctuations in the mix region are correlated by up to ~10% just behind the shock, but these correlations decrease to a fraction of a percent beyond 1 $\mu$m from the shock. The transverse velocity is ~1 $\mu$m/ns for most of the mix region, and the rms variations decay to ~0.4 $\mu$m/ns by a mix-region depth of 4 $\mu$m (see Fig. 100.7). Post-shock turbulence leads to an average excess of kinetic energy in the mix region (as in Ref. 9) of 2%. Figure 100.10 shows the double averages of the density, pressure, the ratio of kinetic energy to total energy (in the pre-shock frame), and $u_y$ for the 16-$\mu$m simulation. Each of these quantities approaches the value predicted by the Rankine–Hugoniot (RH) jump conditions and by the end of the mix region is within a few percent of those values. The pressure in the majority of the mix region is 7.86±0.05 Mbar, 2.5% lower than that of a homogeneous simulation with the same boundary conditions. The density over the same region is 1.47±0.01 g/cc, 1.7% higher than the RH value. Not surprisingly, the small deviation from the RH values results in a shock speed of 56.17±1.7 $\mu$m/ns, which is near the RH shock speed (here it is within 0.1%). The post-shock adiabat $\alpha \sim p\rho^{-5/3}$ deviates from the RH value by a comparably small amount:

$$\delta \ln \alpha = \delta \ln p - \frac{5}{3}\delta \ln \rho \sim -4\%.$$

This deviation from the RH jump conditions is well within the tolerance of high-gain, direct-drive foam designs for the NIF. The main effect of variation in the speed of the first shock is mistiming of the shocks. If the shock is too slow, for instance, then the first two shocks will meet in the inner-fuel regions of the shell, preheating the fuel and compromising target performance. This effect can be simulated in 1-D by deliberately mistiming the first shock, by varying the length of the foot pulse. This is shown for a particular high-gain, wetted-foam NIF target design (see Fig. 100.11).[4] Here a 10% change in shock speed corresponds to a shock mistiming of 300 ps, and

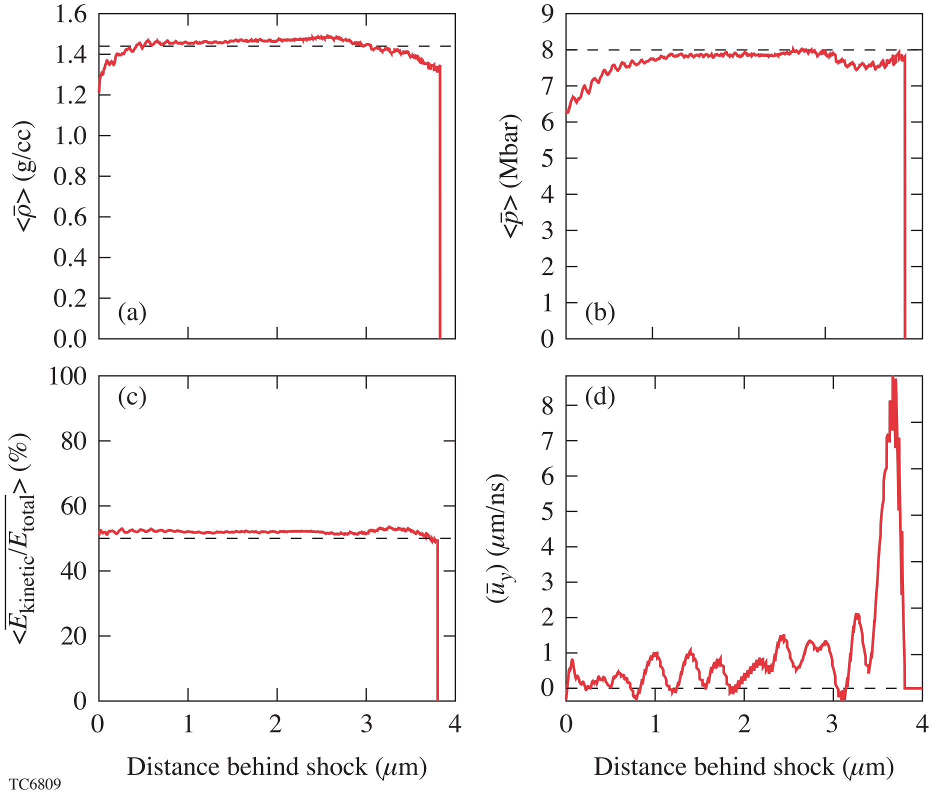

TC6809

Figure 100.10
The time- and space-averaged density (a), pressure (b), ratio of kinetic to total energy (in the pre-shock frame) (c), and vertical velocity (d) as functions of the distance behind the shock front. The values given by the Rankine–Hugoniot jump conditions for a homogeneous mixture of the same density are also shown (dashed lines).

the target shows little change in gain for a mistiming of >400 ps. For this design, at least, this suggests that any change in shock speed due to foam microstructure will have little effect on target performance. While the shock speeds for relevant pressures in DT-wetted plastic foams have yet to be measured experimentally, dry-foam shock speeds have been shown to agree to within experimental error with Rankine–Hugoniot values over a wide range of densities.[30]

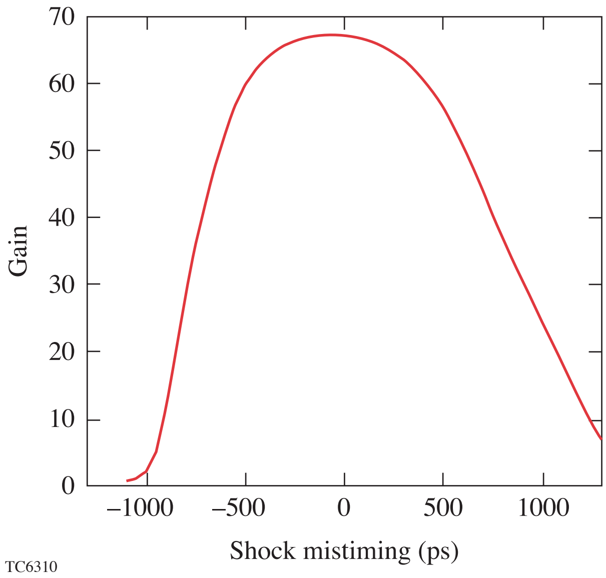

Figure 100.11
The target gain as a function of first-shock mistiming for a high-gain, wetted-foam, direct-drive NIF target design.

As the shock propagates through the wetted-foam layer, the shock front acquires perturbations due to the different shock speeds in the DT and CH [see Fig. 100.3(a)]. Shock-front perturbations are potentially able to seed velocity and surface perturbations on the inner surface of the target shell—a process called *feedthrough*. When the shock reaches the inner shell surface, a rarefaction wave is launched toward the outer surface of the shell. These inner-surface perturbations are carried to the outer surface of the shell by this rarefaction wave—so-called *feedout* (see, e.g., Ref. 31 for a further description of these phenomena). During the acceleration phase as the laser ablation drives the implosion of the shell, the outer surface is subject to the Rayleigh–Taylor instability, which may magnify position and velocity perturbations at the outer shell surface. During the deceleration phase of an implosion, the inner surface is also subject to the Rayleigh-Taylor instability, causing fed-through perturbations to grow, potentially reducing the core temperature and shell areal density and compromising target performance.

The rms variation in the amplitude of shock-front perturbations is shown in Fig. 100.12 for a simulation where the shock has propagated through 5 $\mu$m of wetted foam, into 5 $\mu$m of homogeneous DT (with a transverse simulation size of 0.2 $\mu$m). In the wetted foam, the shock-front perturbations are comparable to a few nanometers. Shock fronts are stable[32] because a concave perturbation leads to a locally converging shock, higher pressure, and higher local shock speed, while a convex perturbation has the opposite effect (see Ref. 33 for further discussion of shock stability). The shock-front stability causes the shock-front perturbations to decay quickly after entering the DT layer, to a level of ~0.1 nm. These levels of nonuniformity are well below the level of the inner-surface shell ice roughness required for direct drive on the NIF.[34]

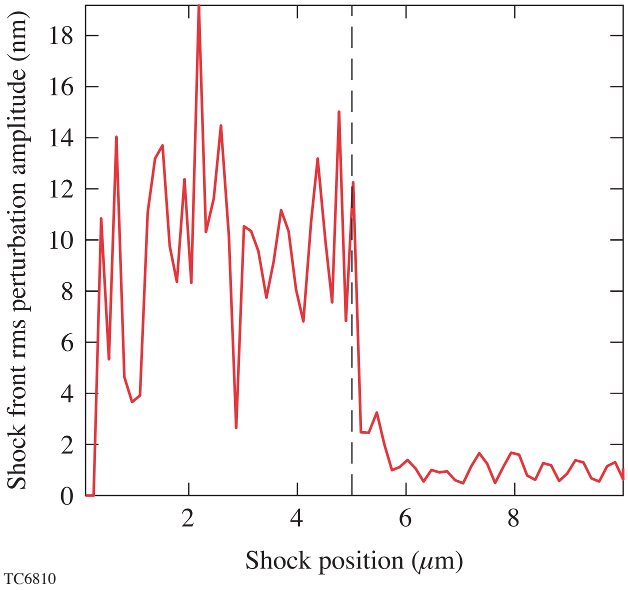

Figure 100.12
The rms shock-front perturbation amplitude as a function of shock position for a simulation consisting of 5 $\mu$m of wetted foam and 5 $\mu$m of DT. The transverse simulation size is 0.2 $\mu$m.

### Results for Different Pushers

We will now consider two different inflow boundary conditions, which correspond to different ablator materials, or "pushers." If these boundary conditions are not the same as the average post-shock conditions in the wetted foam as in the "impedance-matched" conditions used above, then secondary shocks or rarefaction waves will reflect off the wetted foam. To illustrate the role of these reflected waves, we will first consider simulations in which the pusher is post-shock DT. This simulates a wetted-foam shell for which the DT ice overfills the foam shell. This will be followed by a description of simulations of a CH pusher.

The fibers and the DT are in pressure equilibrium before the shock with a pre-shock pressure $p_1$. As the shock, of Mach number $M$ and strength $z$, moves through the DT pusher, it raises the pressure to $p_2 = p_1 (1 + z)$ and, since $z >> 1$ and $\gamma = 5/3$, the density to $\sim 4\rho_{DT}$. When the shock reaches the wetted foam, it encounters a jump in the average density. The strong shock is transmitted into the wetted foam, while a weak shock is reflected back into the DT pusher. The reflected shock further increases the DT pressure to $p_2 + \delta p_2$, where $\delta p_2$ depends on the density ratio and here $\delta p_2 < p_2$. In simulations where the fibers are resolved, this weak reflected shock is made up of the shocks reflected off the individual CH fibers. These reverse shocks are shown in Fig. 100.13, which shows the density averaged over $y$ (transverse to the shock propagation) at a particular time. In this case $p_2 = 3$ Mbar, and $\delta p_2 \sim 0.5$ Mbar. Since the post-shock DT and wetted foam are in pressure equilibrium, this is also the pressure in the post-shock wetted foam. Thus the post-shock pressure in the wetted foam is also higher than $p_2$, the post-shock pressure in the DT pusher. The resulting shock speed is given by $D_i = D_{DT}\left(1 + \delta p_2 / p_2\right)^{1/2}$, where $D_{DT} = \left[4 p_2 / \left(3 \rho_{DT}\right)\right]^{1/2}$ is the shock speed in the DT.

For comparison, if a shock of the same Mach number (i.e., driven by the same pressure used to drive the DT above) is launched into a homogeneous wetted-foam mixture of CH and DT (rather than a DT pusher followed by a layer where the individual fibers are resolved), it will have a shock speed of $D_h = D_{DT}\left(\rho_{DT} / \rho_{ave}\right)^{1/2}$, where $\rho_{ave}$ is the average density of the wetted foam. For $\rho_{DT} < \rho_{ave}$, $\delta p_2 > 0$ and so $D_i > D_h$—i.e., when the shock is driven by a pusher of the same pressure $p_2$ the shock speed in an inhomogeneous mixture exceeds that in a homogeneous mixture. This is seen in Fig. 100.13, which shows $\bar{p}(x)$ and $\bar{\rho}(x)$ for a particular time for homogeneous and inhomogeneous mixtures driven by shocks of the same pressure $p_2$ and the same starting point. The degree by which it exceeds the homogeneous shock speed depends on the average fiber density and, while essentially a 1-D effect, can also be related to the fiber radius.[35]

For a laser-driven shock, this is not the steady-state solution. In this case, the reverse shock, when it reaches the ablation surface, is no longer supported at that pressure, and a rarefaction wave is launched into the target, lowering the

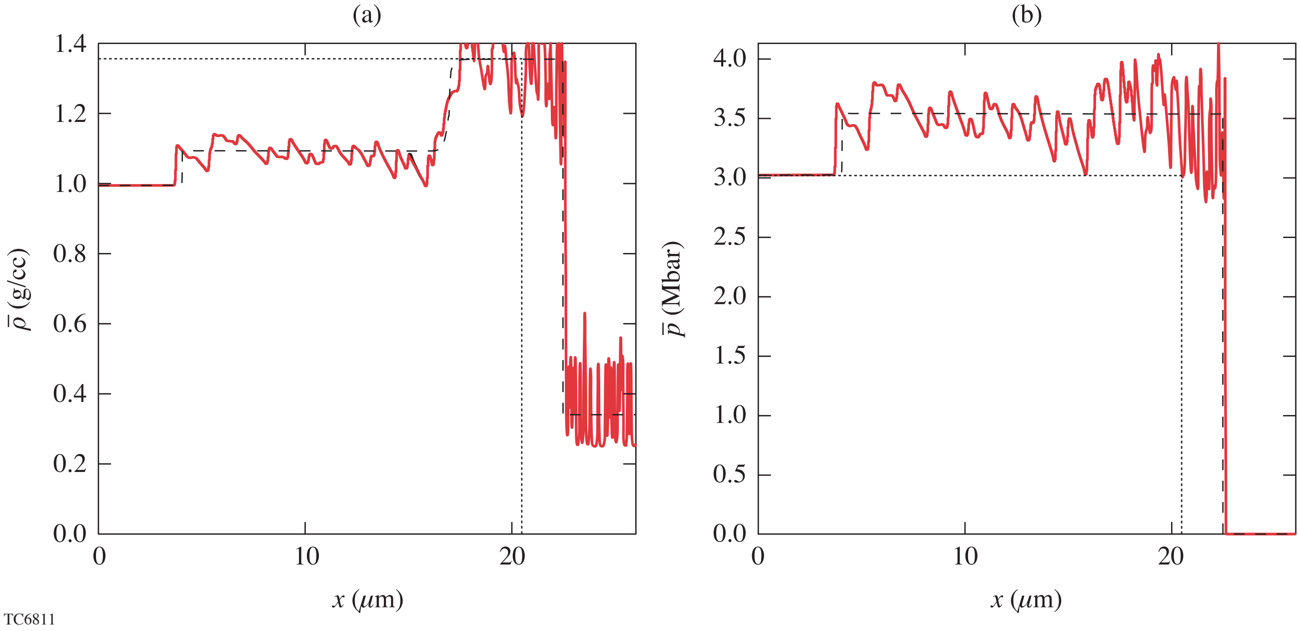

Figure 100.13
The density (a) and pressure (b) as functions of distance for a particular instance in time, for a simulation of a shock driven through wetted foam by a DT pusher. An equivalent homogeneous simulation is shown (dashed) as well as a simulation (dotted) in which pusher and foam are replaced by a homogeneous mixture with the same average density as the wetted foam.

pressure from $p_2 + \delta p_2$ to the ablation pressure, taken here to be $p_2$. The trajectories of the main and reflected shocks are shown in Fig 100.14, in which the inverse of the pressure scale length is plotted for a 1-D simulation of a high-gain, NIF wetted-foam target design with a DT ablator. For this design, this transient shock state persists for 70 ps. The RH jump conditions, which must be obeyed in the case of a homogeneous mixture, are also approximately obeyed for the fiber-resolved simulation (see Fig. 100.13, where the density of the inhomogeneous case is compared to that of a homogeneous case driven with a post-shock pressure $p_2 + \delta p_2$).

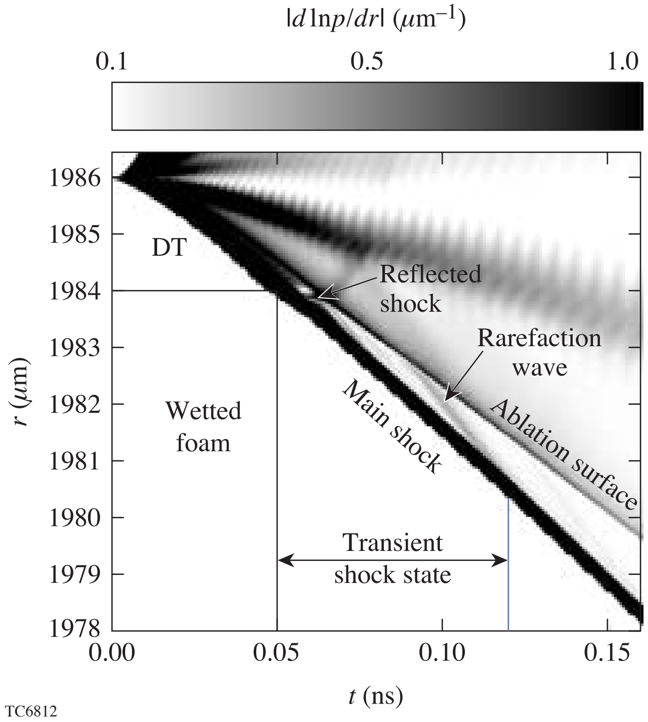

Figure 100.14
The magnitude of the inverse of the pressure scale length for a wetted-foam ignition target design in which the wetted-foam layer is overfilled, forming an external 2-$\mu$m layer of DT. Shocks and rarefaction waves are labeled.

For target fabrication reasons, wetted-foam targets are likely to be constructed with a thin outer layer of CH, the second inflow boundary condition discussed in this section. In this case, the ablator is of higher density than the wetted foam. As a result, when the main shock moves from the CH to the wetted foam, it increases in speed. Because of this, a rarefaction wave is reflected off the interface, rather than a shock. When the RW reaches the ablation surface, where the ablation pressure is determined by the laser energy deposition rate, a weak shock or compression wave is launched back into the target. These waves are shown in Fig. 100.15, which shows the inverse of the pressure scale length for a high-gain, NIF wetted-foam target with a ~2-$\mu$m-CH ablator. In contrast to the case above of the DT pusher, the shock is undersupported until the compression wave reaches it. This transient state lasts for 100 ps in this design. Figure 100.16 shows the $y$-averaged pressure and density compared with a homogeneous simulation also using a CH pusher. This shows again that the RH jump conditions are obeyed, and the average shock speed is approximately the same in both cases.

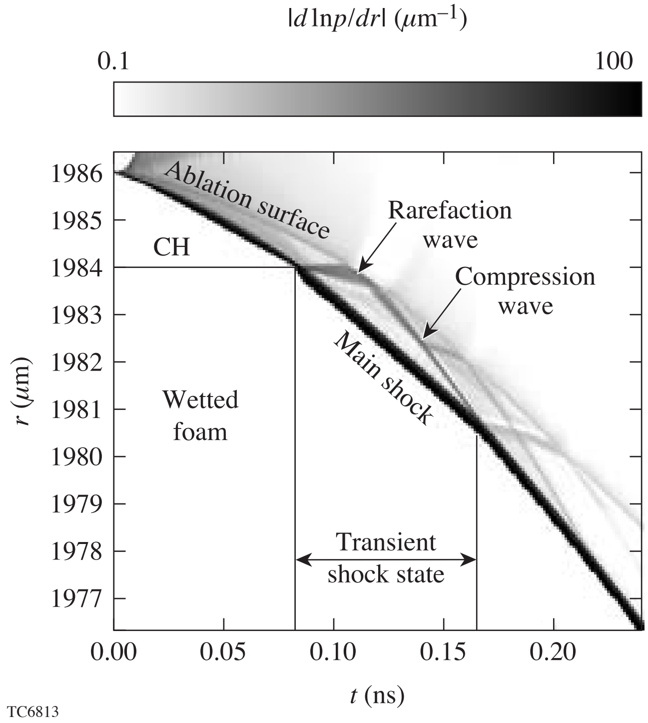

Figure 100.15
The magnitude of the inverse of the pressure scale length for a wetted-foam ignition target design with an external 2-$\mu$m layer of CH.

## Conclusions

High-gain, direct-drive, wetted-foam ICF targets have been designed previously for use on the NIF and in IFE. Due to the prohibitively large range of length scales from the foam microstructure to the pellet size, simulations of these designs generally assume a homogeneous mixture for the wetted foam. We have simulated shock propagation in wetted-foam mixtures. We have found that the size of the decay length behind the shock is of the order of a micron for relevant foam densities. In the mix region, the transverse and turbulent motion decay sufficiently that the Rankine–Hugoniot jump conditions are obeyed to within a few percent. As a result, the average shock speeds are also within a few percent of their homogeneous values. This implies that designs, which are less sensitive than this to shock timing, may be simulated using the approximation of homogeneous mixtures.

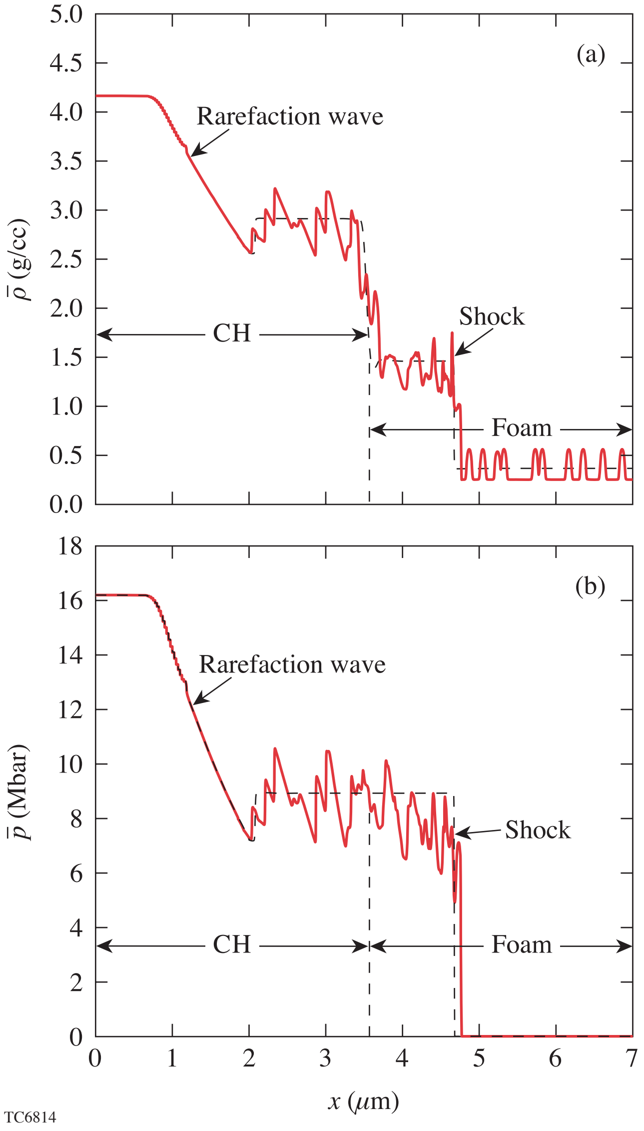

Figure 100.16
The density (a) and pressure (b) as functions of distance are shown for a particular time, along with the values from a simulation of a corresponding homogeneous medium with the same average pre-shock density (dashed). The inflow boundary conditions correspond to a CH pusher.

We have also considered the "lifetime" of shock-front perturbations. As expected, because shock fronts are stable, perturbations seeded by the wetted-foam layer decay quickly after the shock enters the homogeneous DT-ice layer. Therefore we expect the wetted-foam microstructure to have a negligible effect on feedthrough and feedout.

Finally, we have examined the effects of using other "pushers"—DT and CH—to simulate the transient states that occur early in a target overfilled with DT ice and a target with an outer CH overcoat. The RH conditions are also met to within a few percent for these inflow conditions.

## ACKNOWLEDGMENT

The author would like to thank I. Igumenshchev, P. B. Radha, and V. Goncharov for many useful discussions. This work was supported by the U.S. Department of Energy Office of Inertial Confinement Fusion under Cooperative Agreement No. DE-FC52-92SF19460, the University of Rochester, and the New York State Energy Research and Development Authority. The support of DOE does not constitute an endorsement by DOE of the views expressed in this article.

## REFERENCES

1. J. Nuckolls *et al.*, Nature **239**, 139 (1972).
2. L. M. Hair *et al.*, J. Vac. Sci. Technol. A **6**, 2559 (1988).
3. D. G. Colombant *et al.*, Phys. Plasmas **7**, 2046 (2000).
4. S. Skupsky, R. Betti, T. J. B. Collins, V. N. Goncharov, D. R. Harding, R. L. McCrory, P. W. McKenty, D. D. Meyerhofer, and R. P. J. Town, in *Inertial Fusion Sciences and Applications 2001*, edited by K. Tanaka, D. D. Meyerhofer, and J. Meyer-ter-Vehn (Elsevier, Paris, 2002), pp. 240–245.
5. J. D. Sethian *et al.*, Nucl. Fusion **43**, 1693 (2003).
6. M. Desselberger *et al.*, Phys. Rev. Lett. **74**, 2961 (1995).
7. J. D. Lindl, Phys. Plasmas **2**, 3933 (1995).
8. E. M. Campbell and W. J. Hogan, Plasma Phys. Control. Fusion **41**, B39 (1999).
9. L. Phillips, in *Shock Compression of Condensed Matter—1995*, edited by S. C. Schmidt and W. C. Tao (AIP Press, Woodbury, NY, 1996), pp. 459–462.
10. G. Hazak *et al.*, Phys. Plasmas **5**, 4357 (1998).
11. A. D. Kotelnikov and D. C. Montgomery, Phys. Fluids **10**, 2037 (1998).
12. F. Philippe *et al.*, Laser Part. Beams **22**, 171 (2004).

13. B.-I. Jun, T. W. Jones, and M. L. Norman, Astrophys. J. **468**, L59 (1996).

14. A. Y. Poludnenko, A. Frank, and E. G. Blackman, Astrophys. J. **576**, 832 (2002).

15. A. Poludnenko *et al.*, "AstroBEAR: AMR for Astrophysical Applications—I: Methods," to be published in *Adaptive Mesh Refinement—Theory and Applications*.

16. M. J. Berger and R. J. LeVeque, SIAM J. Numer. Anal. **35**, 2298 (1998).

17. R. J. LeVeque, J. Comput. Phys. **131**, 327 (1997).

18. M. Rudman, Int. J. Numer. Methods Fluids **24**, 671 (1998).

19. H. F. Robey, Phys. Plasmas **11**, 4123 (2004).

20. J. G. Clérouin, M. H. Cherfi, and G. Zérah, Europhys. Lett. **42**, 37 (1998).

21. M. C. Richardson, P. W. McKenty, F. J. Marshall, C. P. Verdon, J. M. Soures, R. L. McCrory, O. Barnouin, R. S. Craxton, J. Delettrez, R. L. Hutchison, P. A. Jaanimagi, R. Keck, T. Kessler, H. Kim, S. A. Letzring, D. M. Roback, W. Seka, S. Skupsky, B. Yaakobi, S. M. Lane, and S. Prussin, in *Laser Interaction and Related Plasma Phenomena*, edited by H. Hora and G. H. Miley (Plenum Publishing, New York, 1986), Vol. 7, pp. 421–448.

22. J.-Ch. Robinet *et al.*, J. Fluid Mech. **417**, 237 (2000).

23. A. Y. Poludnenko, K. K. Dannenberg, R. P. Drake, A. Frank, J. Knauer, D. D. Meyerhofer, M. Furnish, J. R. Asay, and S. Mitran, Astrophys. J. **604**, 213 (2004).

24. R. I. Klein, C. F. McKee, and P. Colella, Astrophys. J. **420**, 213 (1994).

25. J. M. Picone and J. P. Boris, J. Fluid Mech. **189**, 23 (1998).

26. N. Cowperthwaite, Physica D **37**, 264 (1989).

27. A. J. Lim and A. C. Raga, Mon. Not. R. Astron. Soc. **303**, 546 (1999).

28. M. M. Maclow *et al.*, Astrophys. J. **433**, 757 (1994).

29. L. D. Landau and E. M. Lifshitz, *Fluid Mechanics* (Pergamon Press, London, 1959).

30. M. Koenig *et al.*, Phys. Plasmas **6**, 3296 (1999).

31. R. Betti, V. Lobatchev, and R. L. McCrory, Phys. Rev. Lett. **81**, 5560 (1998).

32. A. E. Roberts, Los Alamos National Laboratory, Los Alamos, NM, Report LA-299 (1945).

33. G. B. Whitham, *Linear and Nonlinear Waves*, Pure and Applied Mathematics (Wiley, New York, 1974).

34. P. W. McKenty, V. N. Goncharov, R. P. J. Town, S. Skupsky, R. Betti, and R. L. McCrory, Phys. Plasmas **8**, 2315 (2001).

35. T. J. B. Collins, S. Skupsky, V. N. Goncharov, R. Betti, P. W. McKenty, P. B. Radha, R. Epstein, A. Poludnenko, A. Frank, and S. Mitran, in *Inertial Fusion Sciences and Applications 2003*, edited by B. A. Hammel, D. D. Meyerhofer, J. Meyer-ter-Vehn, and H. Azechi (American Nuclear Society, La Grange Park, IL, 2004), pp. 92–95.